Developing equal suspended matter retrieval algorithms from two satellite hyperspectral sensors

Xavier Soria-Perpinyà[1], Bárbara Alvado[1], Gabriel Caballero[1], Antonio Ruíz-Verdú[1], Jesús Delegido[1], Juan Miguel Soria[2], José Moreno[1], María A. Rodrigo Alacreu[2]

[1]Image Processing Laboratory, Parc Científic Universitat de València, Edifici E4, 4a planta, C/Catedrático Agustín Escardino, 9, 46980 Paterna (España), Javier.soria-perpina@uv.es, Barbara.alvado@uv.es, Gabriel.caballero@uv.es, Antonio.ruiz@uv.es, jesus.delegido@uv.es, jose.moremo@uv.es
[2]Cavanilles Institute of Biodiversity and Evolutionary Biology (ICBiBE), Parc Científic Universitat de València, C/Catedrátic José Beltrán Martinez, 2, 46980 Paterna (Espanha), juan.soria@uv.es, maria.a.rodrigo@uv.es.

Keywords: total suspended matter, inorganic matter, organic matter, water quality, PRISMA, EnMAP.

Abstract

The impacts of climate change in the Mediterranean basin are characterized by the alternation between prolonged droughts and episodes of high-intensity torrential rainfall. These hydrometeorological extremes contribute to severe soil erosion, the extent of which is strongly influenced by the land cover within the catchment area, ultimately affecting the quality of the receiving water body. Taking advantage of the increased availability of hyperspectral imagery in recent years, this study aims to estimate both the concentration and composition of suspended matter in inland waters situated in the eastern Iberian Peninsula. For this purpose, we have relied on 55 in situ samples and their respective reflectance spectra, for 36 sites from the L2D product of the PRISMA mission, and for 19 sites from the L2A product of the EnMAP mission. To obtain algorithms, we first use the ARTMO toolbox to identify the best-performing ones and then determine the same retrieval algorithm for both sensors. For the organic fraction the best algorithm uses the 714 nm band, with a NRMSE of 15% for PRISMA and 10% for EnMAP. For the inorganic fraction, the best-performing algorithm was based on the ratio between the ~705 nm band and the 551 nm band, with a NRMSE of 8% for PRISMA and 5% for EnMAP. Finally, the total suspended matter is the sum of both fractions, with a NRMSE of 9% for PRISMA and 5% for EnMAP.

1. Introduction

Total suspended Matter (TSM) is the total mass of suspended particles measured per volume of water, including inorganic (minerals) and organic components (detritus and phytoplankton) (Matthews, 2011). Its presence in aquatic ecosystems influences: light penetration, temperature increase, the transport routes of materials and pollutants, the reduction of dissolved oxygen due to organic decomposition, increased treatment costs, and an unpleasant appearance (Bilotta and Brazier, 2008). Effects that depend on the concentration, composition, particle size, and duration of events that alter TSM (Bilotta and Brazier, 2008).

These events are altered by human activities, which introduce nutrient-rich waters into ecosystems (Paerl et al., 2019), leading to eutrophication, and changing land use, potentially causing erosion (Lunetta et al., 2010). Additionally, the effects of climate change must be considered, as in the Mediterranean basin, it will result in alternating long periods of drought with episodes of high-intensity torrential rains, increasing the importance of reservoirs in water resource regulation.

Currently, the TSM monitoring of surface water bodies can be supported by remote sensing, as TSM represents the suspended portion of the optically active components (OAC) of water, and the interaction of light with TSM produces a signal in water reflectance that can be detected from a remote distance (Bukata, 1995).

Based on this principle, numerous studies have been conducted to develop algorithms for estimating TSM concentration (Adjovu et al., 2023). However, studies aimed at separating the organic and inorganic fractions of TSM are scarce. This is partly due to the low spectral resolution of sensors. Nevertheless, in recent years, the number of hyperspectral sensors, such as PRISMA (2019) and EnMAP (2022), has increased. In fact, PRISMA has already been used to estimate TSM concentration, employing bio-optical models like BOMBER (Bresciani et al., 2022) or performing inversions based on physical models using the WASI processor (Niroumand-Jadidi et al., 2020). While for EnMAP, simulated data have been used to apply machine learning approaches (Saberioon et al., 2023). However, none of these studies have focused on estimating the TSM composition.

Given the greater information about OAC provided by new hyperspectral sensors, they should allow for the estimation of both the concentration and composition of TSM. Therefore, in this study we aim to develop algorithms for estimating suspended matter (concentration and composition) using images from PRISMA and EnMAP sensors. Finally, we compare the algorithms using coincidence images from both sensors over the same water body.

2. Methodology

2.1 Study area

The study area is situated in the eastern Iberian Peninsula, within the western Mediterranean region. Sampling was conducted across seven distinct water bodies (Figure 1), comprising one natural waterbody (l'Albufera) and six artificial reservoirs.

Based on their trophic status, the water bodies can be divided into two groups: eutrophic (turbid waters) and oligotrophic (clear waters). The eutrophic group includes l'Albufera (AL), Bellús (BE), and Beniarrés (BR). L'Albufera de València is part of a Natural Park and is a shallow (1 m), hypereutrophic coastal

lagoon with a hydrological regime regulated for rice cultivation. In contrast, Bellús and Beniarrés have small drainage basins and are located in valleys with significant human presence. The oligotrophic group comprises Benagéber (BG), Contreras (CN), Sitjar (SI), and Tous (TO), which are reservoirs with large, sparsely populated catchment areas.

Figure 1. Location of water bodies.

2.2 Field sampling

Sampling was scheduled to coincide with the acquisition of satellite images. However, the time window between some field samplings and the corresponding images reached up to ±3 days (Schröder et al., 2024), due to the use of archived imagery from satellite missions.

For sampling in reservoirs, an electric outboard motorboat was used, while in l'Albufera, a rented boat was necessary due to restrictions imposed by the Natural Park. Sampling sites were located at a minimum distance of 100 m from the shoreline to avoid mixed pixels (land/water) and to minimize adjacency effects.

Once anchored, the site was georeferenced, and water transparency was measured using a Secchi disk (20 cm Ø). An integrated water sample was then collected down to the Secchi disk depth (SDD), using a Ruttner bottle for shallow SDDs (turbid waters), or a weighted PVC tube (25 mm Ø) for deeper SDDs (clear waters). Samples were stored refrigerated and in the dark during transport to the laboratory, where TSM, its fractions, and chlorophyll-a (Chl_a) concentration were analyzed.

TSM was determined using a gravimetric method (APHA, 1992), with suspended particulate organic matter (SPOM) removed by combustion. The weight difference between total suspended matter (TSM) and suspended particulate inorganic matter (SPIM) was used to estimate SPOM. Chlorophyll-a extraction followed a standard protocol (Shoaf and Lium, 1976), and concentrations were calculated using a spectrophotometric method (Jeffrey and Humphrey, 1975).

2.3 Image processing

A total of 16 hyperspectral images were used for this study: 9 from the PRISMA sensor (PRecursore IperSpettrale della Missione Applicativa) and 7 from the EnMAP sensor (Environmental Mapping and Analysis Program). The main characteristics of the PRISMA and EnMAP sensors are shown in Table 1.

	PRISMA	EnMAP
Launch	22 March 2019	1 April 2022
Coverage	70º N to 70º S	80º N to 80º S
Target lifetime	5 years	5 years
Spatial resolution	30 m	30 m
Temporal resolution	6 days	4 days
Number of bands	66 VNIR 173 SWIR	101 VNIR 123 SWIR
Bandwidth	≤12 nm	≤10 nm

Table 1. Principal specifications of PRISMA (Bresciani et al., 2022; Niroumand-Jadidi et al., 2020) and EnMAP (Chabrillat et al., 2024) sensors.

The images used in this study included the atmospheric correction provided by each mission: the L2D product from PRISMA and the L2A product from EnMAP. These products were selected based on the good validation results of reflectance against in situ data obtained for our study area, which we presented at previous conferences (Alvado et al., 2024; Sòria-Perpinyà et al., 2024).

Reflectance data for each sampling site were extracted by calculating the mean value within a 3×3 pixel window centred on the in-situ sampling coordinates. This process was carried out using the SNAP (Sentinel Application Platform) software, which can directly open EnMAP images. In the case of PRISMA images, originally in HE5 format, they were first opened in QGIS using the EnMAP-Box plugin and exported to .TIF format to be subsequently processed in SNAP. Once reflectance values were obtained, they were converted to Rrs (remote sensing reflectance) by dividing the values by π.

Table 2 provides a summary of the image acquisition and field sampling details, including the sampled water bodies, the associated sensor images, the time interval between field sampling and image acquisition, and the number of sampling sites per sensor for each water body.

Water body	Sensor	Time window	Sites
l'Albufera	PRISMA	2	11
		3	5
	EnMAP	0	3
		2	2
Bellús	PRISMA	0	3
		1	4
		2	2
	EnMAP	0	3
Benagéber	PRISMA	0	3
	EnMAP	0	3
Beniarrés	PRISMA	0	2
		2	3
	EnMAP	0	2
Contreras	PRISMA	0	3
Sitjar	EnMAP	0	3
Tous	EnMAP	0	3

Table 2. Details of water bodies and sensors corresponding to sampling sites.

2.4 Algorithm retrieval

With the aim of treating the variables jointly and ensuring coherence among their estimations, SPIM and SPOM were

estimated separately, and TSM was subsequently be derived as the sum of both components.

The algorithms were initially developed using the ARTMO (Automated Radiative Transfer Models Operator) toolbox, specifically the Spectral Index tool, applying the leave-one-out cross-validation method. Rrs values—whether as single bands, band ratios, or normalized differences—were related to field data using five fitting functions: linear, power, exponential, logarithmic, and polynomial.

Subsequently, algorithms with good validation statistics shared by both sensors were selected. The following validation metrics were considered: R^2, RMSE, RRMSE, NRMSE, MAE, and MAPE. Additionally, to provide physical meaning to the selection of empirical algorithms, the shape of the reflectance spectra was analyzed—particularly in the absorption and scattering regions associated with phytoplankton, water, and SPIM.

$$RMSE = \sqrt{\frac{\sum_{i=1}^{N}(x_i^{estimated} - x_i^{measured})^2}{N}} \quad (1)$$

$$RRMSE = \frac{RMSE}{\sum_{i=1}^{N} x_i^{measured}/N} \times 100 \quad (2)$$

$$NRMSE = \frac{RMSE}{x_{max.}^{measured} - x_{min.}^{measured}} \times 100 \quad (3)$$

$$\mathrm{MAE} = \frac{\sum_{i=1}^{n}|x_i^{estimated} - x_i^{measured}|}{N} \quad (4)$$

$$\mathrm{MAPE} = \frac{\sum_{i=1}^{n}|(x_i^{estimated} - x_i^{measured})/x_i^{measured}|}{N} \times 100 \quad (5)$$

The reflectance spectra used from each sensor are shown in the Results section (Figure 2). However, based on the literature, it is known that phytoplankton exhibits a minimum absorption around 560 nm and a maximum absorption near 665 nm, while the peak scattering occurs around 700 nm. Additionally, an inflection in the scattering curve occurs near 700 nm due to water absorption, resulting in a sharp reflectance peak in highly scattering waters (i.e., turbid or productive waters) (Matthews, 2011). Moreover, both the height and position of this peak have been shown to correlate well with Chl_a concentration, with the peak shifting toward longer wavelengths (~715 nm) as Chl_a increases (Gitelson, 1992). Between 550 and 600 nm—a region of low phytoplankton absorption—Pierson and Strömbeck (2001) reported a relationship between SPIM concentration and increased reflectance.

To enhance the robustness of the algorithm, the selected indices were recalibrated using all available data, excluding the values matched with both sensors. Finally, the algorithms were applied to the images from both sensors acquired over Bellús on July 23, 2024. For comparison purposes, validation statistics were calculated using the three in situ sampling sites collected on the same day, which had not been used in the development of the algorithms.

3. Results and discussion

A total of 55 georeferenced sampling sites were obtained from the 16 field campaigns, including data on TSM, SPIM, SPOM, Chl_a, and SDD. Among these, 36 sites matched with PRISMA imagery and 19 with EnMAP imagery (Table 2). Descriptive statistics for the databases (DBs) associated with each sensor are presented in Table 3.

The data suggests that both DBs are highly similar, as reflected by their median values, and with a broad distribution range, as indicated by their minimum and maximum values. Nonetheless, the PRISMA DB displays a greater concentration of high OAC values, as evidenced by the mean values—except in the case of SDD.

Sensor		TSM (mg/L)	SPOM (mg/L)	SPIM (mg/L)	Chl_a (µg/L)	SDD (m)
PRISMA	Mean	44.34	26.13	18.21	122.53	1.21
	Med.	20.84	14.48	8.37	64.45	0.40
	Max.	192.5	84.38	108.13	491.24	7.10
	Min	1.39	0.79	0.60	0.70	0.10
	S.D.	50.25	26.61	26.02	121.81	1.99
EnMAP	Mean	32.58	19.17	13.41	61.97	2.21
	Med.	20.46	14.43	5.92	37.25	0.45
	Max.	136.0	78.73	75.40	317.33	7.80
	Min	1.76	0.09	0.98	0.62	0.16
	S.D.	42.58	24.69	19.19	90.00	2.76

Table 3. Descriptive statistics of sampled parameters. Med. (Median), Max. (Maximum), Min. (Minimum), S.D. (Standard deviation).

To examine the relationships between variables, Spearman's correlation was applied, as the data did not meet the normality assumption. The results, presented in Table 4, indicate a strong association among all variables (p-value < 0.001) for both DBs. Key differences include that, in the PRISMA DB, the SPOM fraction shows a stronger correlation with TSM, whereas in the EnMAP DB, the strongest correlation is with SPIM. Although SPIM is the suspended matter variable most strongly correlated with Chl_a in general, in the PRISMA DB, the correlation coefficient between SPOM and Chl_a is similarly high, while in the EnMAP DB it is notably lower.

DB		SPOM	SPIM	Chl_a	SDD
PRISMA	TSM	0.984	0.961	0.916	-0.971
	SPOM		0.923	0.926	-0.966
	SPIM			0.933	-0.907
	Chl_a				-0.889
EnMAP	TSM	0.906	0.981	0.945	-0.920
	SPOM		0.867	0.867	-0.891
	SPIM			0.977	0.877
	Chl_a				0.855

Table 4. Spearman correlations coefficients of two DB. All correlations have a $p < 0.001$.

After examining the ranges of the different variables in the DBs and their mutual correlations, we proceeded to analyze how these variables influence the reflectance spectra received by the sensors. Figure 2 shows the 36 PRISMA Rrs spectra and the 19 EnMAP spectra, arranged according to their corresponding TSM values.

By representing the spectra as a function of TSM concentration, two distinct regions can be identified where reflectance increases with TSM levels, with differences noticeable even at low concentrations. These regions correspond, on the one hand, to the spectral inflection around 700 nm, associated with maximum phytoplankton backscattering and water absorption, and on the other, to the 550–600 nm range, which represents the minimum phytoplankton absorption. Notably, the five PRISMA spectra with the highest reflectance differ clearly from the rest. These spectra correspond to an image over l'Albufera de València, captured during an exceptional phytoplankton bloom,

This contribution has been peer-reviewed. The double-blind peer-review was conducted on the basis of the full paper.
https://doi.org/10.5194/isprs-annals-X-3-W3-2025-93-2026 | © Author(s) 2026. CC BY 4.0 License.

where the absorption minimum appears at 600 nm instead of the typical 560 nm.

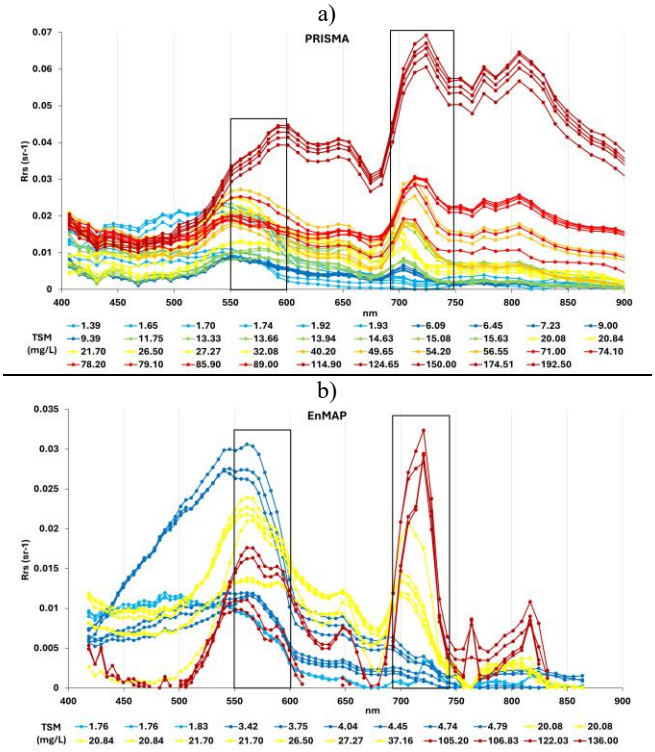

Figure 2. Rrs spectra of sampling sites from PRISMA (a) and EnMAP (b) images. Boxes mark peaks of interest

All of this leads to the conclusion that we are working with waters where phytoplankton is the main OAC. This is especially evident in the PRISMA DB, where 30 samples show Chl_a concentrations above 20 µg/L, while only 6 samples fall below 4 µg/L. In contrast, the EnMAP DB includes 10 samples with Chl_a > 20 µg/L and 9 samples with Chl_a ≤ 6 µg/L.

3.1 Retrieval algorithms

ARTMO presents the results in a separate table for each variable; however, in this study we only report the results of the algorithms selected based on the established criteria: ARTMO performance, indices shared by both sensors, and physical consistency.

As we have observed, in our DBs the OAC that predominantly modifies the reflectance spectrum is phytoplankton. This is the main constituent of the organic fraction, as indicated by the strong correlation between Chl_a, and SPOM.

For this reason, the index for the SPOM variable should be composed of one of the bands that form the peak around 700 nm, bands between 693 and 744 nm, covering the peak shift as TSM increases. Considering all this, the best algorithm was obtained using the band centred at 714 nm for the calibration fit (Figure 3). It is linear for PRISMA with an R^2 of 0.91 and an intercept at the origin to avoid negative estimates (Eq. 6), and follows a power function for EnMAP, with an R^2 of 0.97 (Eq. 7).

$$SPOM_{PRISMA}\left(\frac{mg}{L}\right) = 1299 \times 713.7\ Rrs \quad (6)$$

$$SPOM_{EnMAP}\left(\frac{mg}{L}\right) = 21596 \times 713.5\ Rrs^{1.6422} \quad (7)$$

For the validation fits (Figure 3), the R^2 was 0.91 for PRISMA and 0.98 for EnMAP, with both regression lines positioned below the 1:1 line. The validation statistics can be seen in Table 5, with all metrics being lower for the EnMAP database except for the MAPE of the organic fraction, which was notably high due to three data sites below 1 mg/L from the Benagéber reservoir. Therefore, algorithms used to determine the organic fraction tend to be less accurate in waters where the reflectance spectrum is dominated by inorganic material. For instance, see the three blue spectra with a peak at 550 nm in Figure 2b.

		RMSE mg/L	RRMSE %	NRMSE %	MAE mg/L	MAPE %
PRISMA	SPOM	12.43	46	15	8.89	52
	SPOM*	8.39	42	13	5.44	38
	SPIM	9.05	47	8	5.51	42
	TSM	16.78	36	9	10.87	38
	TSM*	12.23	42	14	7.52	33
EnMAP	SPOM	7.77	39	10	4.60	89
	SPIM	3.34	23	5	2.40	35
	TSM	7.27	21	5	4.39	17

*With EnMAP SPOM algorithm applicated to 31 PRISMA data.

Table 5. Validation metrics for both sensors.

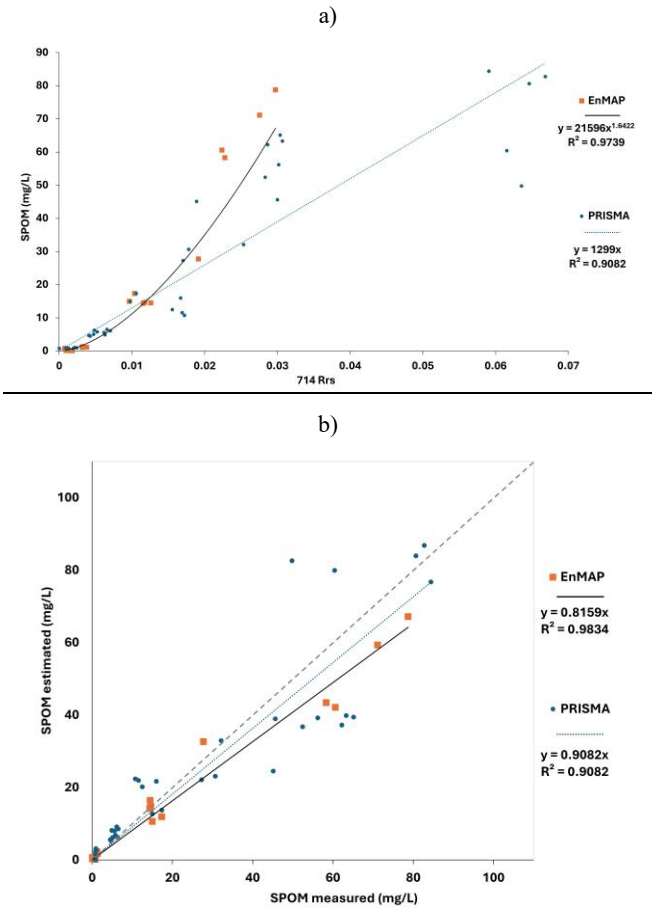

Figure 3. SPOM algorithm calibration (a) and validation (b). Line 1:1 dotted grey line.

Examining the calibration fits, we observe that both DBs lie along the power fit obtained for the EnMAP database, except for the five PRISMA sites with higher reflectance corresponding to data from l'Albufera, which exhibit reflectance spectra above the rest. Given this, we decided to apply the algorithm derived for EnMAP to the PRISMA DB

and calculate the validation statistics excluding the five l'Albufera data sites. Table 5 shows that the validation results improve compared to those obtained using the PRISMA algorithm, including the error percentages.

Regarding the SPIM variable, the best index was obtained using a ratio between a band near 705 nm and a band located at 501 nm. This can be explained by two reasons: first, the strong correlation between SPIM and Chl_a, which justifies the presence of the band around 705 nm at the beginning of the phytoplankton scattering peak; and second, the region of minimal phytoplankton absorption between 550 and 600 nm, where Pierson and Strömbeck (2001) found a relationship between increased reflectance and SPIM concentration.

Thus, the best calibration results were obtained with exponential fits (Figure 4). For PRISMA, the bands centered at 703.7 and 550.9 nm were used (Eq. 8), with an R^2 of 0.91. Meanwhile, for EnMAP, the bands centered at 706.6 and 550.7 nm were used (Eq. 9), with an R^2 of 0.98.

$$SPIM_{PRISMA}\left(\frac{mg}{L}\right) = 0.5591 \times e^{2.7962 \times \frac{703.7\ Rrs}{550.9\ Rrs}} \quad (8)$$

$$SPIM_{EnMAP}\left(\frac{mg}{L}\right) = 1.9906 \times e^{1.6858 \times \frac{706.6\ Rrs}{550.7\ Rrs}} \quad (9)$$

Regarding the validation fits (Figure 4), the R^2 was 0.94 for PRISMA and 0.99 for EnMAP, with both regression lines closely aligned to the 1:1 line. However, the validation statistics (Table 5) were all, without exception, lower for the EnMAP data. It is important to note, nevertheless, that the EnMAP fit intercepts the y-axis at approximately 2 mg/L, which represents the detection limit of the algorithm, whereas the PRISMA algorithm is capable of estimating values below 1 mg/L.

This is mainly due to six samples with SPIM concentrations between 3 and 4 mg/L—three from the Benagéber reservoir and three from the Sitjar reservoir—both characterized by a strong presence of micro-calcites. These micro-calcites increase reflectance around 550 nm, and although they may also enhance reflectance in the NIR region, this increase is more moderate (Schalles et al., 1997). As a result, the ratio value is lower than expected for the corresponding SPIM concentration.

Finally, the validation results are presented for TSM estimated from the sum of equations 6 and 8 for PRISMA, and from the sum of equations 7 and 9 for EnMAP. The validation fits are shown in Figure 5, with an R^2 of 0.94 for PRISMA and an R^2 of 0.99 for EnMAP, with both regression lines closely aligned to the 1:1 line. Like the SPIM results, all validation statistics (Table 5), without exception, are lower for the EnMAP data.

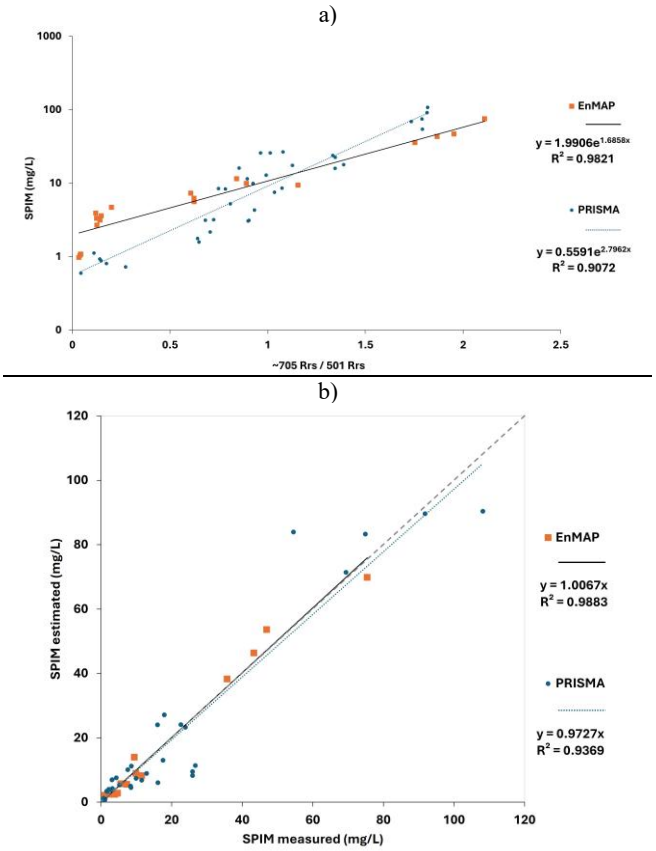

Figure 4. SPIM algorithm calibration (a) and validation (b). Line 1:1 dotted grey line.

Since we had SPOM values estimated using the algorithm derived for EnMAP, TSM values were also calculated from these. In this case, the validation results (Table 5) improved for RMSE and MAE, but not for the percentage errors, likely due to excluding the highest values from the PRISMA database.

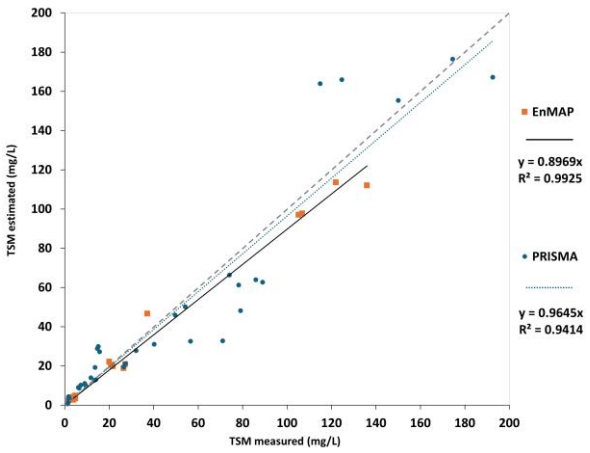

Figure 5. TSM validation. Line 1:1 dotted grey line.

To conclude this section, we examine how hyperspectral sensors improve the accuracy of estimation algorithms. For this purpose, three studies were selected: one conducted in the same study area but with a different data range, and two from different study areas but with similar data ranges.

In the study carried out in the same area (Alvado et al., 2021), using the multispectral Sentinel-2 sensor, TSM (30–0.6 mg/L), SPOM (6–0.4 mg/L), and SPIM (13–0.2 mg/L) were estimated with normalized RMSE (NRMSE) values of 10%, 15%, and 12%, respectively. These error percentages are higher than those obtained in the present study, which involved much broader data ranges.

Regarding studies conducted in other areas but with comparable data ranges, only TSM estimation studies were found. Using the Sentinel-2 sensor, Gao et al. (2021) reported an RMSE of 14.96 mg/L for a data range of 40 to 90 mg/L. Our results were lower using the algorithm derived from the EnMAP DB, while the RMSE of the algorithm with the PRISMA DB was 16.78 mg/L. Meanwhile, Wang et al. (2022), using in situ radiometry and a range of 1 to 500 mg/L, obtained an RMSE of 16.3 mg/L.

It is important to note that our TSM estimation is performed indirectly through separate estimations of its organic and inorganic fractions.

3.2 Comparative

On July 23, 2024, we obtained a simultaneous overpass of PRISMA and EnMAP over Bellús, where we were able to collect three samples on the same day. Before comparing the validation statistics for these three sites, it is necessary to understand the differences between the acquisition conditions of the two images (Table 6).

Sensor	Time	SZA	SAA	OZA	OAA
PRISMA	11:02	23.7	138.5	11.2	283.3
EnMAP	11:13	22.4	145.0	23.1	13.2

Table 6. Conditions of image acquisition. Time, Solar Zenith Angle (SZA), Solar Azimuth Angle (SAA), Observation Zenith Angle (OZA) and Observation Azimuth Angle (OAA) are extracted from the metadata of the image.

These conditions show that the main difference between the images is the Observation Azimuth Angle (OAA). The OAA indicates that EnMAP is positioned to the east, while PRISMA is positioned to the west, looking towards the sun and therefore with a higher probability of sunglint, as observed in Figure 6.

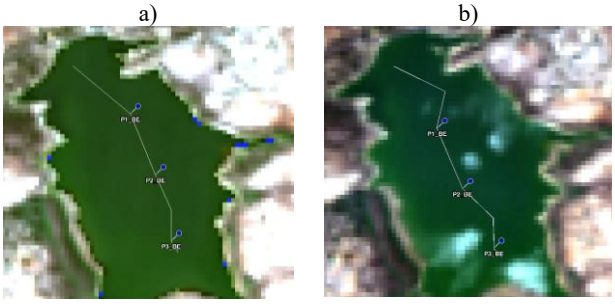

Figure 6. RGB composition images of Bellús 23/07/2024, from EnMAP (a) and PRISMA (b). Sampled sites and extracted transect are indicated.

As shown in Figure 6, information was extracted both from the sampling sites and from the transect running from the tail to the dam, passing through these sites. The data from the sampling sites will be used to calculate the validation statistics (Table 7). The transect will allow us to observe the spatial variation within the reservoir and the effect of sunglint, despite efforts to minimize it by adjusting the transect in the PRISMA image to avoid it.

		RMSE mg/L	RRMSE %	MAE mg/L	MAPE %
PRISMA	SPOM	3.71	26	3.51	24
	SPOM*	5.17	36	4.71	33
	SPIM	2.69	42	2.52	38
	TSM	2.23	11	1.55	8
	TSM*	3.64	17	2.19	11
EnMAP	SPOM	1.12	8	0.74	5
	SPIM	1.08	17	0.81	12
	TSM	1.64	8	1.47	7

*With EnMAP SPOM algorithm applicated to PRISMA data.

Table 7. Validation metrics for both sensors using the sampling set from Bellús 23/07/2024.

In the validation metrics shown in Table 7, we observe that all errors are lower than those obtained during the development of the algorithms. However, in this case, applying the EnMAP algorithm to the PRISMA image did not improve the errors for either SPOM or TSM, unlike what was observed with the data used for developing the PRISMA algorithms. NRMSE results are not presented because the difference between the maximum and minimum values is very small, resulting in a very high NRMSE.

In the tail-to-dam transect shown in Figure 7, we can see that the PRISMA algorithms tend to underestimate SPIM and overestimate SPOM, thereby achieving better TSM estimates. Greater variability is also observed compared to the EnMAP transects, likely due to sunglint effects. Despite the overall homogeneity of the reservoir, the cleansing effect of reservoirs can be observed, with decreasing concentrations toward the dam, except in the final section.

Although based on a limited number of sites and without identical acquisition conditions, the comparison has proven effective in assessing the consistency of the results and confirming that the selected bands are key for retrieving the organic and inorganic fractions of suspended matter in water bodies where the dominant OAC is the phytoplankton.

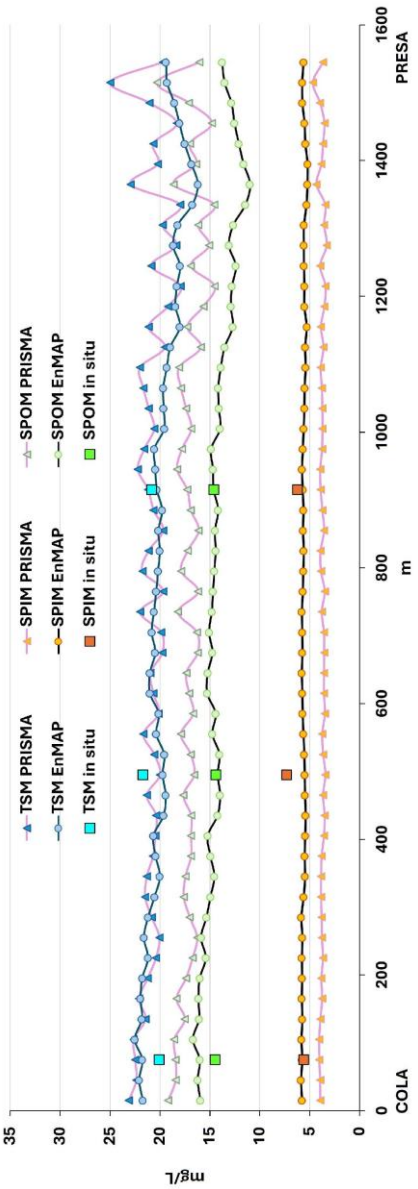

Figure 7. Tail-to-dam transect from Bellús 23/07/2024 images. TSM, SPOM, and SPIM variables along with the corresponding in situ measurements.

4. Conclusions

Phytoplankton is the main OAC influencing the reflectance spectrum in our database. The results show that the adjusted algorithms depend greatly on the DB from which they are derived.

The best algorithm for estimating the SPOM variable is based on the band centered at 714 nm, which lies at the inflection point between the peak scattering by phytoplankton and the increasing absorption by water. Reaching a RMSE of 12,43 mg/L and NRMSE of 15% for PRISMA and a RMSE of 7.77 mg/L and NRMSE of 10% for EnMAP. But these algorithms tend to be less accurate in waters where the reflectance spectrum is dominated by inorganic material.

The best algorithm for SPIM is a ratio between a band near 705 nm and a band located at 551 nm, the first marking the onset of maximum phytoplankton scattering, and the second corresponding to the region of minimum phytoplankton absorption. Achieving a RMSE of 9,05 mg/L and NRMSE of 8% for PRISMA and a RMSE of 3.34 mg/L and NRMSE of 5% for EnMAP.

As demonstrated by the comparative analysis, the algorithms developed for both PRISMA and EnMAP are consistent and accurate when applied to imagery within the study area.

The results indicate that empirical algorithms developed using hyperspectral sensors are more accurate than those derived from multispectral sensors.

These findings could serve as a reference for the development of suspended matter algorithms for upcoming missions, including the Italian PRISMA Second Generation in 2025, NASA's Surface Biology and Geology mission from 2028, and the ESA Copernicus Hyperspectral Imaging Mission for the Environment (CHIME), planned for 2029.

5. Acknowledgments

The authors acknowledge the project CIPROM/2021/49, intitled Remote Sensing Spectroscopy for wetlands BIOdiversity (RESSBIO), funded by the PROMETEU program of the Generalitat Valenciana.

References

Adjovu, G.E., Stephen, H., James, D., Ahmad, S., 2023. Overview of the application of remote sensing in effective monitoring of water quality parameters. *Remote Sens.*, 15(7),1938(35).

Alvado, B., …, Moreno, J. Comparación entre ACOLITE y productos L2 de los sensores PRISMA, DESIS y EnMAP en aguas interiores. In Proceedings of the XX *Congreso de la Asociación Española de Teledetección*, Cádiz, Spain, 5–7 June 2024.

APHA, 1992: Standard methods for the examination of water and wastewater. 18th edition. American Public Health Association. Washington D.C., USA. 1105 pp.

Bilotta, G.S., Brazier, R.E., 2008. Understanding the influence of suspended solids on water quality and aquatic biota. *Water Res.*, 42(12), 2849-2861.

Bresciani, M., Giardino, C., Fabbretto, A., Pellegrino, A., Mangano, S., Free, G., Pinardi, M., 2022. Application of new hyperspectral sensors in the remote sensing of aquatic ecosystem health: Exploiting PRISMA and DESIS for four Italian lakes. *Resources*, 11(2), 8(17).

Bukata, R.P., 1995. The effects of chlorophyll, suspended mineral, and dissolved organic carbon on volume reflectance. Optical Properties and Remote Sensing of Inland and Coastal Waters, 135-166.

Chabrillat, S., Foerster, S., Segl, K., Beamish, A., Brell, M., Asadzadeh, S., ..., Fischer, S., 2024. The EnMAP spaceborne imaging spectroscopy mission: Initial scientific results two years after launch. *Remote Sens. Environ.*, 315, 114379.

Gao, Z., Shen, Q., Wang, X., Peng, H., Yao, Y., Wang, M., ..., Liang, W., 2021. Spatiotemporal distribution of total suspended matter concentration in Changdang Lake based on in situ

hyperspectral data and sentinel-2 images. *Remote Sens.*, 13(21), 4230.

Gitelson, A., 1992. The peak near 700 nm on radiance spectra of algae and water: relationships of its magnitude and position with chlorophyll concentration. *Int. J. Remote Sens.*, 13, 3367–3373.

Jeffrey, S.T., Humphrey, G.F., 1975. New spectrophotometric equations for determining chlorophylls a, b, c1 and c2 in higher plants, algae and natural phytoplankton. *Biochem. Physiol. Pflanz.*, 167, 191-194.

Lunetta, R.S., Shao, Y., Ediriwickrema, J., Lyon, J.G, 2010. Monitoring agricultural cropping patterns across the Laurentian Great Lakes Basin using MODIS-NDVI data. *Int. J. Appl. Earth Obs. Geoinf..,* 12, 81–88.

Matthews, M.W., 2011. A current review of empirical procedures of remote sensing in inland and near-coastal transitional waters. *Int. J. Remote Sens.*, 32(21), 6855-6899.

Niroumand-Jadidi, M., Bovolo, F., Bruzzone, L., 2020. Water quality retrieval from PRISMA hyperspectral images: First experience in a turbid lake and comparison with sentinel-2. *Remote Sens.*, 12(23), 3984.

Paerl, H.W., Havens, K.E., Hall, N.S., Otten, T.G., Zhu, M., Xu, H., Zhu, G., Qin. B, 2019. Mitigating a global expansion of toxic cyanobacterial blooms: confounding effects and challenges posed by climate change. *Mar. Fresh. Res.*, 71, 579-592.

Pierson, D.C., Strömbeck, N., 2001. Estimation of radiance reflectance and the concentrations of optically active substances in Lake Mälaren, Sweden, based on direct and inverse solutions of a simple model. *Sci. Total Environ.*, 268(1-3), 171-188.

Saberioon, M., Khosravi, V., Brom, J., Gholizadeh, A., Segl, K., 2023. Examining the sensitivity of simulated EnMAP data for estimating chlorophyll-a and total suspended solids in inland waters. *Ecol. Inform*., 75, 102058.

Schröder, T., Schmidt, S.I., Kutzner, R.D., Bernert, H., Stelzer, K., Friese, K., Rinke, K., 2024. Exploring Spatial Aggregations and Temporal Windows for Water Quality Match-Up Analysis Using Sentinel-2 MSI and Sentinel-3 OLCI Data. *Remote Sens.*, 16(15), 2798(22).

Schalles, J.F., Schiebe, F.R., Starks, P.J., Troeger, W.W., 1997. Estimation of algal and suspended sediment loads (singly and combined) using hyperspectral sensors and integrated mesocosm experiments. In Proceedings of the Fourth International Conference on Remote Sensing of Marine and Coastal Environments, Orlando, Florida, March 17–19, 1997, vol. 1, pp. 247–258

Shoaf, W.T., Lium, B.W., 1976. Improved extraction of chlorophyll a and b from algae using dimethyl sulphoxide. *Limnol. Oceanogr.*, 21, 926-928.

Sòria-Perpinyà, X., …, Rodrigo, M.A. Assessment of atmospheric correction algorithms in PRISMA, DESIS, and EnMAP images in inland waters. In Proceedings of the EARSeL, València, Spain, 16–19 April 2024.

Wang, X., Song, K., Liu, G., Wen, Z., Shang, Y., Du, J., 2022. Development of total suspended matter prediction in waters using fractional-order derivative spectra. *J. Environ. Manag.*, 302, 113958.